Title

Precision measurement of relative γ -ray intensities from the decay of 61Cu

Authors

Bleuel, DL

Bernstein, LA

Marsh, RA

et al.

Publication Date

2021-04-01

DOI

10.1016/j.apradiso.2021.109625

Peer reviewed

Applied Radiation and Isotopes 170 (2021) 109625

Contents lists available at ScienceDirect

Applied Radiation and Isotopes

journal homepage: www.elsevier.com/locate/apradiso

Precision measurement of relative γ-ray intensities from the decay of ^{61}Cu

D.L. Bleuel [a,*], L.A. Bernstein [b,c], R.A. Marsh [a], J.T. Morrell [c], B. Rusnak [a], A.S. Voyles [c]

[a] Lawrence Livermore National Laboratory, Livermore, CA 94551, USA
[b] Lawrence Berkeley National Laboratory, Berkeley, CA 94720, USA
[c] University of California, Berkeley, CA 94720, USA

ARTICLE INFO

Keywords:
γ ray intensity
^{61}Cu
Cross section
β^+ decay
Electron capture

ABSTRACT

A discrepancy, well outside reported uncertainties, has been observed between the accepted and measured values of the intensity ratio of the two strongest γ rays following ^{61}Cu β^+ decay. This discrepancy has significant impact since the ^{nat}Ni(d,x)^{61}Cu reaction has historically been one of only a few IAEA recommendations for use as a deuteron flux monitor and a considerable number of published cross sections measured in ratio to that beam monitor cross section may depend on the choice of either the first or second strongest γ ray in those calculations. To determine the magnitude of this error most precisely, over a hundred separate measurements of the 283 keV to 656 keV γ-ray emission ratio were collected from seven experiments and a variety of detectors and detection geometries. A weighted average of all these measurements indicates an error in the value listed in the Nuclear Data Sheets of 11% in either the primary or second-highest intensity γ ray of ^{61}Cu, potentially introducing an 11% error in ^{61}Cu production cross section measurements, cross sections using nickel activation as a deuteron beam current monitor, or in dose rates when ^{61}Cu is used in nuclear medicine. General agreement with the Data Sheets with ten other intensity ratios suggests the most probable error is in the secondary (656 keV) emission, which accordingly should be updated from 10.8% to 9.69%.

1. Introduction

The radionuclide ^{61}Cu and its γ-ray emissions are of high importance to several fields. Notably, its production in the ^{nat}Ni(d,x)^{61}Cu reaction is recommended by the International Atomic Energy Agency (IAEA) as a deuteron beam current monitor (Hermanne et al., 2018). Nickel, along with aluminum, titanium, iron and copper, is one of only five such materials recommended by the IAEA and the ^{nat}Ni(d,x)^{61}Cu reaction is one of only a handful of reactions with an energy threshold below about 10 MeV. A collection of measurements of this cross section along with an evaluation using a Padé statistical approach, is shown in Fig. 1. The ^{nat}Cu(p,x)^{61}Cu reaction (Shahid et al., 2015; Graves et al., 2016; Garrido et al., 2016; Červenák and Lebeda, 2020) is often similarly used as a proton beam monitor, though not specifically recommended by the IAEA.

Furthermore, ^{61}Cu has characteristics deemed advantageous in nuclear medicine, such as in positron emission tomography (PET) (McCarthy et al., 1999; Williams et al., 2005; Ruangma et al., 2006), and is typically considered as a shorter-lived (and thus lower dose) theranostic pair with ^{67}Cu to replace ^{64}Cu. A number of reactions have been identified for the production of ^{61}Cu for medical use (Aslam and Qaim, 2014b,a; Qaim, 2019), each of which relies on accurate nuclear data for quantification. Incorrect production cross section data or an inaccurate isotopic survey could adversely impact patient doses.

Regardless of use or reaction, precision production cross sections very often rely on measuring one or more characteristic γ rays in an activated material, usually in a high-resolution detector such as high-purity germanium (HPGe). Typically, the strongest γ ray, i.e. the one with the highest intensity multiplied by detector efficiency, is used to achieve the lowest statistical counting uncertainty. However, often an average of similarly-strong γ rays may also be used. Cross sections measured in this way use the known intensities and uncertainties for each γ ray, listed for ^{61}Cu in Table 1, from the Nuclear Data Sheets (Zuber and Singh, 2015) (NDS).

Hereafter, γ-ray emissions will be referred to in this text by only three significant digits for brevity except when additional precision is needed, though the full values were used in analysis. For ^{61}Cu, both the most intense γ ray emission and highest detection probability in a typical HPGe detector is 282.956(10) keV (hereafter referred to as 283 keV, or the primary emission) which, according to the NDS, is emitted in 12.2(22)% of β^+ decays. The second is at 656.008(10) keV (hereafter 656 keV, or the secondary emission), that is emitted with 88.3(15)% of the intensity of the 283 keV γ ray, and whose absolute intensity shares the systematic uncertainty of the 283 keV

* Corresponding author.
E-mail address: bleuel1@llnl.gov (D.L. Bleuel).

https://doi.org/10.1016/j.apradiso.2021.109625
Received 28 October 2020; Received in revised form 19 January 2021; Accepted 26 January 2021
Available online 11 February 2021

Table 1
Relative intensities (I_γ) of γ rays of energy E_γ observed in this study, per 100 decays of the primary emission (283 keV), from the Nuclear Data Sheets (NDS) (Zuber and Singh, 2015). For absolute intensity per 100 decays, multiply by 0.122(22).

E_γ	I_γ
67.412(10)	34.7(11)
282.956(10)	100.0
373.050(10)	17.6(4)
529.169(22)	3.1(1)
588.605(10)	9.57(17)
656.008(10)	88.3(15)
816.692(13)	2.52(6)
841.211(17)	1.75(5)
902.294(20)	0.68(4)
908.631(17)	9.0(2)
1099.560(19)	2.01(5)
1132.351(32)	0.737(34)
1185.234(15)	30.6(6)
1446.492(19)	0.37(2)

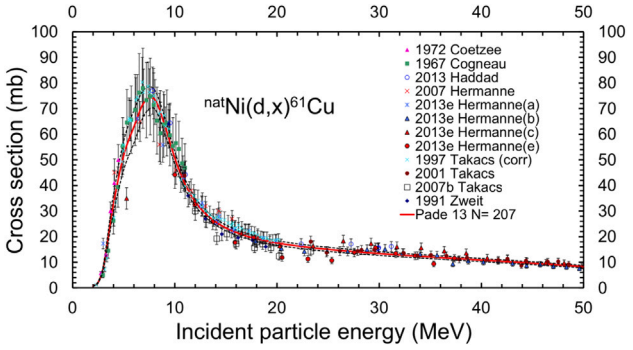

Fig. 1. (Color online) Experimental and evaluated cross sections for the ^{nat}Ni(d,x)^{61}Cu reaction from Hermanne et al. (2018).

emission. Although the most recent NDS evaluation of these transition intensities was compiled in 2015, the quantities have been based on only a single Ref. (Satyanarayana et al., 1988) from thirty years prior (though the NDS erroneously cites a different source, Meyer et al. (1978), from ten years earlier). This is despite older, conflicting measurements (Satyanarayana et al., 1988; Meyer et al., 1978; Grütter, 1982; Ritter and Larson, 1969; Schöneberg and Flammersfeld, 1967; Bolotin and Fischbeck, 1967; Béraud et al., 1967) that are summarized in Table 2. It is readily apparent that great discrepancies exist in these initial measurements.

Possibly in response to an early notification of this study (Singh, 2019), the ENSDF library (ENSDF, 2020) was recently updated with a re-evaluation of the intensities of ^{61}Cu γ-rays. Although no additional data were available as of this or the 2015 evaluation, the inclusion of a greater number of historical sources in the evaluation led to a reduction in the secondary-to-primary intensity ratio to 0.82, also included in Table 2. Although all intensities have been normalized to the 656 keV emission, the uncertainty of this decay has been assigned a value (17%) approximately an order of magnitude larger than in the NDS, which was normalized to the 283 keV emission. The comments indicate that the reduced χ^2 of these intensity ratios from the different publications significantly exceeds the critical value, presumably contributing to this large uncertainty and further necessitating more precise measurements. This re-evaluation has not yet been published in the NDS at the time of this publication.

In several recent publications (Gyürky et al., 2019; Cvetinović et al., 2015), the half life of ^{61}Cu was re-examined but the γ-ray intensities were not. In a very recent measurement of the ^{nat}Cu(p,x)^{61}Cu cross section, it was noted (Červenák and Lebeda, 2020) that a 656/283 keV ratio of 76.0% was more consistent with their observations than the NDS value. There are indications (Nelson et al., 2017) that the decay

Table 2
Measured intensity, I_γ of 656 keV γ-ray emissions from ^{61}Cu decay, relative to 283 keV emission, in percent, from listed references.

Reference	I_γ (%)
Satyanarayana et al. (1988)	88.34(1.52)
Grütter (1982)	79.3(1.9)
Meyer et al. (1978)	85.3(20)
Ritter and Larson (1969)	88.7(6.1)
Schöneberg and Flammersfeld (1967)	77.7(3.4)
Bolotin and Fischbeck (1967)	67.7(4.8)
Béraud et al. (1967)	91.4(12.9)
ENSDF (2020)	82.0(14.3)

of ^{61}Cu was observed in Gammasphere prior to 2017, but this data has not yet been published at the time of this article.

In our recent experiments at Lawrence Berkeley National Laboratory's (LBNL's) 88-Inch Cyclotron, a substantially different 656 keV to 283 keV intensity ratio from ^{61}Cu decay, activated from ^{nat}Ni(d,x)^{61}Cu reactions in nickel beam monitor foils, was observed compared to the NDS value. To add confidence in this observation, over a hundred different HPGe measurements of the 283 keV, 656 keV, and other characteristic γ rays were collected from seven different experiments, 40 foils, several reaction mechanisms, three different detectors, and at various distances from each detector. Unfortunately, as positrons were not detected in any of these experiments, only the ratio of characteristic γ ray intensities to the primary 283 keV emission was determined. Although in most cases, the total production of ^{61}Cu could be calculated from the reaction cross section shown in Fig. 1, that published cross section's reliance on the respective γ-ray intensities would have resulted in circular reasoning.

Cross section evaluations based on studies with different methodologies would be adversely affected by a large error in the primary to secondary γ-ray intensities. Furthermore, it is not always established unambiguously in the literature which γ rays were used in the determination of ^{nat}Ni(d,x)^{61}Cu cross sections. For instance, in the three measurements by Takács et al. (1997, 2001, 2007) shown in Fig. 1, the 1997 and 2007 publications only tabulate the secondary 656 keV γ-ray as a characteristic emission, while the 2001 study includes both the 283 keV and 656 keV data without explicitly identifying which was used (or if some linear combination). Communication with the author (Takács, 2020) indicated that the choice of 656 keV, when made, was to avoid room background influences at 283 keV. Coetzee and Peisach (1972) specify that "the 284 keV photopeak" was used, but is limited to the ^{60}Ni(d,n)^{61}Cu reaction lower than 5.5 MeV. The age of this publication predates most of the measurements in Table 2 and it is unclear if values were adjusted in the evaluation for a more modern normalization. Zweit et al. (1991) specifies use of the 283 keV γ ray. Cogneau et al. (1967), measuring only below 12 MeV, detected the β^+ emission directly with thresholding absorbers to differentiate activation products. However, these values were decreased by 38% in the evaluation to fit with other measurements and are thus influenced by those other publications' choices of γ ray. The reference for F. Haddad is simply "private communication, to be published" and thus the choice of γ ray is unknown. It is therefore unclear to what degree the recommended ^{nat}Ni(d,x)^{61}Cu cross section, and others based upon it, have been affected.

2. Experiments

2.1. Facilities/experiments

As previously noted, over a hundred γ-ray measurements were compiled from seven different experiments which used thin (~25 μm) nickel or copper activation foils, such that self-shielding effects were insignificant, as proton or deuteron beam monitors. A summary of these experiments is listed in Table 3. All experiments were performed at

LBNL's 88-Inch Cyclotron (Kireeff Covo et al., 2018) except for Exp. 3, which was performed at Los Alamos National Laboratory's (LANL) Isotope Production Facility (IPF). With the exception of Exp. 2, the primary motivation of each experiment was not to study ^{61}Cu decay. However, every effort was made to re-analyze each dataset consistently.

For the LBNL experiments (Exp. 1,2, and 4–7), four detectors were used. The primary detector, designated "Rm131-Det2", is a 46.2% efficient (for 1332 keV γ rays, relative to a 3"x3" NaI detector at 25 cm) ORTEC GMX Series (model #GMX-50220-S) HPGe detector enclosed in thick lead shielding when counting at distances less than 19 cm. At further distances, the top of this shielding enclosure must be opened. The remaining detectors at LBNL are three unshielded "Interchangeable Detector Modules" (IDM-200V's), designated IDM1, IDM2, and IDM3. Counts were made at varying times after irradiation, between 0.5–12 h, generally for short time frames (1–30 min) relative to the 3.339(8) hour half life of ^{61}Cu (Zuber and Singh, 2015).

For the LANL experiments (Exp. 3) irradiated at the IPF, calibration and peak fitting were performed by the Nuclear Radiochemistry Group in the LANL Technical Area-48 (TA-48) Countroom, who also calculated and reported uncertainties. The calibration procedure and uncertainty analysis described in the following section applies only to the LBNL experiments.

A small, environmental background at 282.92(5) keV can be present, from the decay of ^{235}U in concrete and other structures. While the intensity of this γ ray per ^{235}U decay is only 0.0060(6)%, it may contribute to the 283 keV γ-ray peak over a long count time in an unshielded environment. However, for each detector configuration, background measurements much longer than the count times of the ^{61}Cu measurements indicated no detectable contribution from this or other background sources.

For the unshielded IDM detectors, however, a detectable background interference with the 121 keV γ ray from ^{152}Eu was observed and subtracted from calibration data. This environmental γ ray was detected at a rate of $\sim 0.77\gamma$/s, about 2% of the peak from a ^{152}Eu source when measured at ~30 cm. No such background interference was observed on other detectors, which were in better-shielded environments.

2.2. Detector calibration

2.2.1. Relative efficiency curve fitting

Since only ratios of γ-ray emissions from ^{61}Cu decay were determined, the highest-precision relative efficiency calibration was more important than absolute accuracy. For that reason, with the exception of Exp. 3, only ^{152}Eu sources were used, to eliminate uncertainties from systematic differences in the absolute activities of multiple calibration sources. The Fitzpeaks (2014) code was used for all γ ray photopeak fitting, while a custom python routine using the non-linear least squares scipy.optimize.curve_fit function was written to interpolate photopeak detection efficiency, ϵ, between the 11 strongest measured γ-ray emissions of ^{152}Eu, using the formula,

$$\ln \epsilon = \sum_{i=0}^{4} a_i \ln(E_\gamma)^i, \quad (1)$$

where a_i are fit parameters and E_γ is the γ-ray energy. In some cases, the peak at 1086 keV was excluded when it was thought that the uncertainty added from differentiating the doublet of overlapping peaks in this region outweighed the relative benefit of including it in the fit.

Two uncertainties associated with this functional fit procedure were calculated, described in the next two sections: a "fit variability" due to the statistical uncertainties of the measured ^{152}Eu γ rays, and an "interpolation error" from the accuracy of interpolating with Eq. (1), even with a perfect ^{152}Eu calibration.

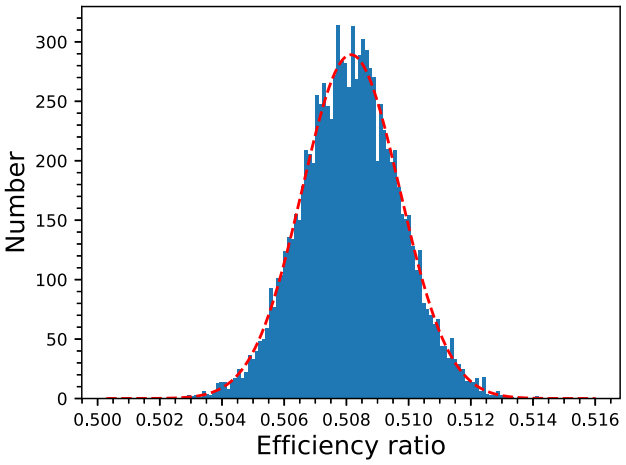

Fig. 2. (Color online) Example distribution (from Exp.4, Det.5) of 10,000 interpolated 656–to–283 keV efficiency ratios when input points are perturbed within a normal distribution about their means.

2.2.2. Fit variability

To propagate the uncertainty in this fit from the statistical uncertainties in the ^{152}Eu peak counts, a Monte Carlo method was used, refitting 10,000 perturbed efficiency curves for each detector configuration. Each peak activity was sampled from a normal distribution about its measured value with width characterized by its count and peak integral uncertainty. The standard deviation from the ratio of the interpolated efficiency at each γ-ray energy in ^{61}Cu to the primary peak (283 keV) was then used as the energy-dependent fit variability uncertainty. One example of the distribution of this ratio with perturbed input parameters, for samples measured 15.2 cm (Det.5) from the Rm131-Det2 detector in Exp.4, is shown in Fig. 2. From this distribution, this detector configuration's 656/283 keV efficiency ratio is determined to be 0.5081 with a fit variability uncertainty of 0.0015.

2.2.3. Interpolation error

To quantify the uncertainty in the interpolation accuracy of the efficiency fit function itself, two methods were utilized: comparison to a MCNP (Werner et al., 2018) simulation of the HPGe detector and a deleted-residuals analysis. Due to the large number of detector configurations and reliance on limited, past calibration data, these procedures were carried out only on a single detector configuration, in which the statistical count uncertainties were extremely small due to a very long simulation or calibration count (~2 days of a ~1 μCi ^{152}Eu source), minimizing the "fit variability" previously described. This uncertainty was then applied to each data set, regardless of detector or geometry.

For the Room131-Det2 detector at 18.2 cm, this "long count" fit function was compared against MCNP simulations of the detector, shown in Fig. 3, in which the distance to the γ-ray source, dead-layer thickness, and crystal length were adjusted to match the efficiencies determined by the ^{152}Eu source and a ^{133}Ba source. This ^{133}Ba source contribution was made strictly to provide relative low-energy datapoints at 53, 80, and 81 keV as guidance for the dead layer thickness optimization and not used in the fit to Eq. (1). It was found that inclusion of any of these low-energy data points to fit parameters only affects extrapolated efficiency values below 121 keV and does not significantly affect (<0.1%) any interpolated values between 121 keV and 1408 keV.

A comparison of the measured ^{152}Eu photopeak efficiencies with the functional fit and MCNP simulation for measurements taken at 18.2 cm is shown in Fig. 4. Fit uncertainties generated by the methodology outlined in Section 2.2.2 are shown at points corresponding to major γ-ray emissions from ^{61}Cu decay.

Table 3
Experiments (and references when published) which produced ^{61}Cu activation samples in this study, indicating experiment dates, laboratory locations, ^{61}Cu-producing reactions, primary beam energy, number of foils, number of measurements (some foils were counted multiple times), the detector used (see text for descriptions), the distance from the front face of each detector casing, a detector configuration identification for the detector and distance combination. When single foils were counted on multiple detectors, the number of foils was only indicated for the first detector (resulting in some empty rows).

Designation	Date	Loc.	React.	E_{beam}	Foils	Meas.	Detector	Distance	Det.ID
Exp.1	Dec. 2016	LBNL	d+Ni	16 MeV	4	4	Rm131-Det2	12.2 cm	Det.1
Exp.2	Nov 2019	LBNL	d+Ni	16 MeV	3	3	Rm131-Det2	18.2 cm	Det.2
					1	1	IDM1	20.8 cm	Det.4
Exp.3[a]	Jan 2017	LANL	p+Cu	41–99 MeV	6	12	TA-48	12.4 cm	Det.9
Exp.4[b]	Feb 2019	LBNL	d+Ni	7–31 MeV	5	5	Rm131-Det2	15.2 cm	Det.5
					5	5	Rm131-Det2	18.2 cm	Det.6
						3	IDM2	31.4 cm	Det.7
						1	IDM3	53.1 cm	Det.8
Exp.5[c]	Dec 2016	LBNL	p+Cu	55 MeV	5	5	Rm131-Det2	14.2 cm	Det.10
						5	Rm131-Det2	29.5 cm	Det.13
Exp.6[d]	Aug 2017	LBNL	p+Cu	35–57 MeV	4	20	Rm131-Det2	18.2 cm	Det.17
					6	30	Rm131-Det2	15.2 cm	Det.18
						10	Rm131-Det2	5.2 cm	Det.19
Exp.7	Aug 2018	LBNL	d+Ni	16 MeV	1	3	Rm131-Det2	39.6 cm	Det.12
TOTAL					40	107			

[a] Voyles et al. (2018).
[b] Ekeberg (2020).
[c] Voyles et al. (2019).
[d] Morrell et al. (2020).

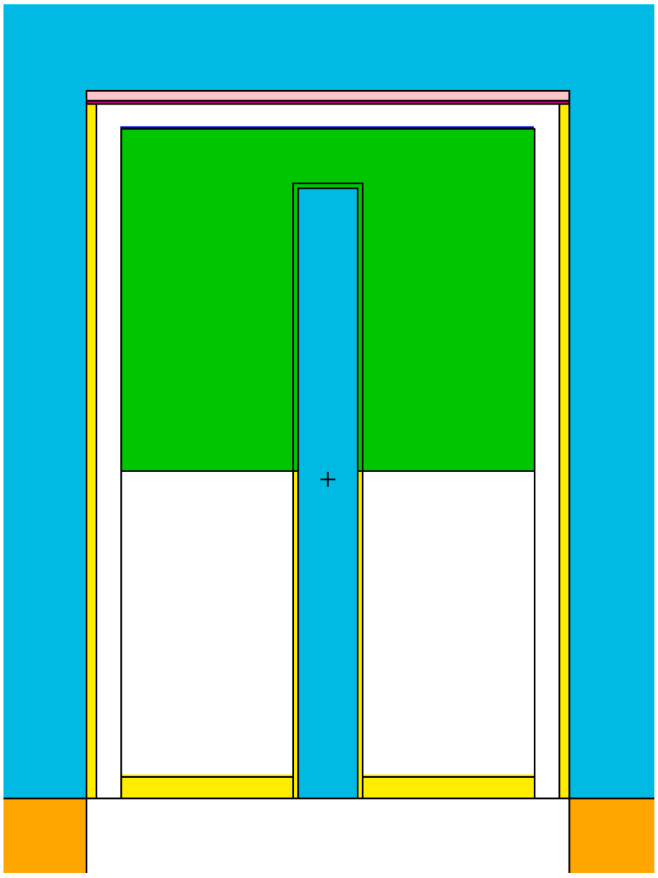

Fig. 3. Cross section (cylindrically symmetric about the y axis) of an MCNP model of the Room131-Det2 HPGe detector, including a 53.8 mm long by 32.45 mm diameter HPGe crystal (green) with a 35 μm Ge dead layer below 5 μm mylar insulation, a 0.5 mm beryllium window (red) with a 1.4 mm plastic cap (pink), aluminum housing (yellow), and lead shielding (orange). Most of the lead enclosure is not shown. (For interpretation of the references to color in this figure legend, the reader is referred to the web version of this article.)

This MCNP model is somewhat simplified (e.g. lacking crystal edge curvature, interior geometry assessment, and borehole characterization) but sufficient for interpolating a physically-relevant, energy-dependent detector response for comparison with the functional fit. The agreement between simulation and fit to within 1% corroborates the second methodology of uncertainty assessment.

For the second methodology, the fit to Eq. (1) was performed using the same long-count ^{152}Eu source measurements. This fit was then repeated eight times without including the contribution from one of each of the γ rays between 344–1112 keV. Due to the decaying-exponential shape of the curve, it was assumed that these more-restricted fits would not be realistically comparable to the complete fit without contributions from the first two and last γ rays, especially as intensities are calculated in ratio to the primary 283 keV emission from ^{61}Cu. The interpolated efficiencies from these more-restricted fits were then compared to the measured values of the excluded points. The ratio of the measured efficiency from these γ rays to that of the full efficiency curve fit, along with the same ratio of the omitted γ rays to the restricted efficiency curve fits is shown in Fig. 5.

The deviation of each measurement from these restricted fits are extremely close to their deviation from the full fit in Fig. 4b. The standard deviation from unity is 0.88% with no significant positive or negative bias (the mean residual is equal to −0.1%) or clear energy dependence. The data demonstrates slightly better correlation with the MCNP prediction than the fit, but the energy dependence of the MCNP model may reflect affects of the fact that the model was adjusted by hand rather than through more rigorous minimization techniques. The lack of a definitive energy dependence in the observed deviations of measured efficiencies from the fit indicated no discernable covariance in the interpolation uncertainties. Therefore the quadrature sum of the standard deviation with itself ($\sqrt{2} \times 0.0088$), accounting for the numerator and denominator of each intensity ratio, was applied as a systematic uncertainty to every intensity ratio at all energies. This value of 1.2% is conservatively consistent with the differences in both the measured data and the functional fit with the MCNP model, seen in Fig. 4c,d. A summary of the uncertainties discussed is presented in Table 4.

Furthermore, the long count time allowed the observation of lower-intensity (<0.5% of decays) γ-ray emissions from ^{152}Eu closer in energy to those from ^{61}Cu decay, such as 296 keV (near 283 keV) and 586 keV (near 656 keV), although still to only ~1%–2% accuracy. While a minor-intensity γ-ray conveniently exists in ^{152}Eu at 656 keV, our

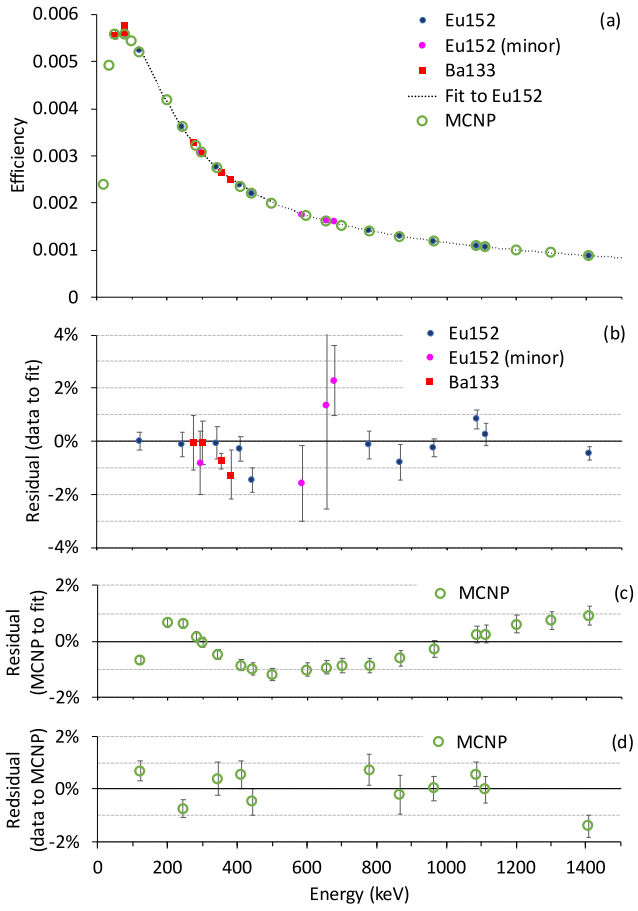

Fig. 4. Representative efficiencies (a) generated for the Room131-Det2 detector from sealed sources measured at 18.2 cm from the detector, showing a functional fit (dashed line) to Eq. (1) between 121–1408 keV to the 11 major γ-ray emissions of ^{152}Eu (blue circles). Also shown are those from ^{133}Ba (red squares), some minor emissions of ^{152}Eu (magenta circles), and an MCNP simulation (green open circles). Residuals are shown between 121–1408 keV of the difference between (b) the measured data and the functional fit, (c) the MCNP simulation and the functional fit, and (d) the measured data and the MCNP simulation. Error bars in (a) and (b) include 1σ activity statistical and γ-ray *relative* intensity, in (c) include only simulated statistical, and in (d) activity statistical, relative emission, and simulated statistical uncertainties. Where not depicted, they are smaller than the datapoint. (For interpretation of the references to color in this figure legend, the reader is referred to the web version of this article.)

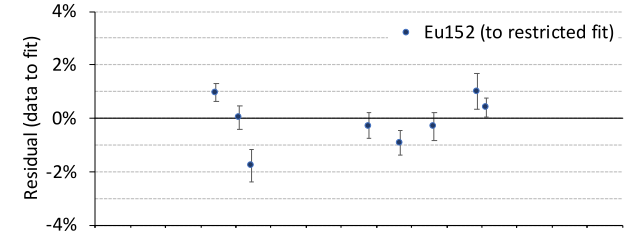

Fig. 5. (Color online) Residuals of each measured efficiency to restricted functional fit when datapoint is removed from fit.

measurement at that value over two days was only accurate, after background subtraction, to 3.6%. Much longer count times than two days are subject to energy calibration drift and comparable signal-to-background and do not necessarily improve the accuracy. While not used for efficiency curve fits, these are also shown in Fig. 4 as a confirmation of the interpolation accuracy. For the minor-intensity energies (296 and 586 keV), the deviation is on order or less than their

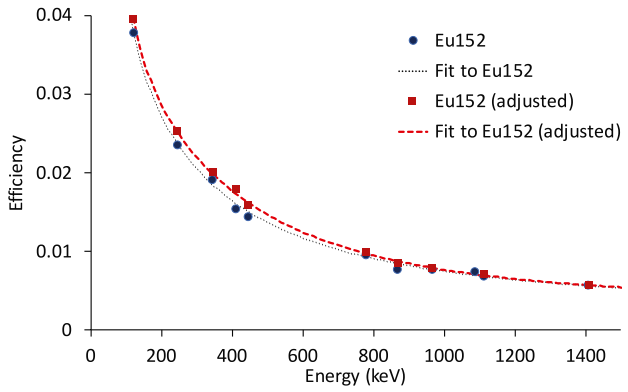

Fig. 6. Measured efficiency (datapoints) and fitted curves (dotted lines) before (blue) and after (red) adjustment for coincident summing effects for Det.19 (the only case where effects were significant). Error bars are smaller than the datapoints. (For interpretation of the references to color in this figure legend, the reader is referred to the web version of this article.)

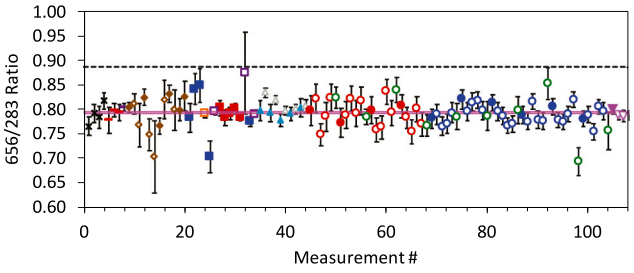

Fig. 7. (Color online) Ratio of the 656 keV γ-ray intensity to that of the 283 keV γ ray emitted from ^{61}Cu. Data symbols indicate each experiment, in order from left to right, listed in Table 3 while colors represent a particular detector/distance combination. Open data symbols indicate that the same sample was measured as the previous, either repeated or on a new detector configuration. Error bars are 1σ statistical only. The dashed black line shows the NDS value while the magenta line shows the weighted mean of these measurements (line thickness representing 1σ weighted statistical uncertainty of 0.001).

Table 4
Uncertainties applied to intensity ratios.

Uncertainty	Range
Counting/peak fit statistical	Varies (<10%)
Efficiency fit variability	0.2–2.1%
Efficiency fit interpolation accuracy	1.2%

~1% measurement uncertainties, added in quadrature to the systematic efficiency fit interpolation uncertainty described.

2.2.4. *Coincident summing*

The decay of activation foils or calibration sources leading to γ ray emission often proceeds through a complicated decay scheme in which multiple γ rays may be emitted in coincidence with each other. If such sources are placed relatively close to a detector such that the possibility of full or partial energy deposition from two or more simultaneously-emitted γ rays is not negligible, "coincidence summing" effects can occur. This can either lead to a decrease in the observed γ-ray photopeak, or when the fully-photoabsorbed energies of multiple, consecutive γ rays matches that of a non-coincident emission, an increase.

The effect of coincidence summing was calculated, using the technique of Semkow et al. (1990) implemented in a FORTRAN program written by Brune et al. (1994). Using the full decay scheme of both ^{152}Eu and ^{61}Cu, both "summing in" and "summing out" corrections are calculated for each photopeak. Angular correlations are expected

Table 5
Ratios of γ-ray intensities, in percent, at energy E_γ relative to the intensity at 283 keV. NDS (Zuber and Singh, 2015) and the recent 2020 ENSDF re-evaluation (ENSDF, 2020) values are included for comparison with the weighted means as well as the reduced χ^2 of the data from this mean. All measurements' uncertainties reflect counting/peak fitting and "fit variability" uncertainties, each considered statistical and used solely in the calculation of the weighted mean and reduced χ^2, as well as a 1.24% "efficiency interpolation" uncertainty, which was treated as systematic and added in quadrature to the final weighted mean uncertainty.

#	Det.	E_γ (keV)										
		373.050	529.169	588.605	656.008	816.692	841.211	902.294	1099.560	1132.351	1185.234	1446.492
1	Det.1	16.7(9)	3.1(5)	8.2(7)	76.5(21)	2.5(5)	1.8(5)				30.7(13)	
2	Det.1	15.3(9)	2.9(5)	9.0(7)	79.2(22)	2.5(5)	2.6(5)		2.4(5)		29.3(15)	
3	Det.1	17.8(11)	2.6(6)	8.3(9)	78.4(25)	3.2(6)	2.1(6)		3.7(8)		30.1(16)	
4	Det.1	15.7(8)	2.9(5)	10.0(6)	81.7(21)	2.4(5)	3.0(6)		2.9(7)		30.7(12)	
5	Det.2	17.8(15)		8.3(13)	77.7(29)	3.2(10)					28.2(23)	
6	Det.2	16.2(7)	2.6(7)	7.2(7)	79.8(18)	1.7(6)					30.2(12)	
7	Det.2	15.6(10)	3.4(8)	8.7(8)	79.3(20)	2.0(7)					32.1(16)	
8	Det.4	17.1(6)	2.8(3)	9.3(3)	80.3(13)	2.5(4)	2.5(3)		2.7(7)		29.1(8)	
9	Det.9	16.7(6)		9.4(5)	80.3(14)						29.1(8)	
10	Det.9	16.9(13)		9.2(11)	81.0(23)						29.2(16)	
11	Det.9				77(5)						26(3)	
12	Det.9	18.8(10)		7.2(8)	82.3(19)						32.8(14)	
13	Det.9	13.2(24)			75(3)						23.2(27)	
14	Det.9				70(7)							
15	Det.9	17.9(10)		7.3(8)	76.6(19)						27.5(14)	
16	Det.9	19.1(29)		11.4(23)	82(4)						25(3)	
17	Det.9	16.8(11)		7.3(9)	83.1(21)						26.4(14)	
18	Det.9	23(3)			80(4)						35(4)	
19	Det.9	16.3(15)		7.6(13)	79.8(24)						30.4(20)	
20	Det.9	16.2(20)			83(3)						28.6(28)	
21	Det.5	14.7(17)		9.4(16)	78(3)						28(3)	
22	Det.5	17.1(18)		9.0(17)	84(3)						29(3)	
23	Det.5	16.2(20)		8.7(19)	85(4)						33(3)	
24	Det.8	17.4(5)	3.00(26)	9.1(3)	79.0(18)	2.42(27)	1.80(29)	0.78(25)			28.3(8)	
25	Det.5	17.1(19)		7.2(18)	70(3)						27(3)	
26	Det.7	17.2(4)	2.95(21)	8.8(3)	79.4(18)	2.65(24)	2.03(26)				29.6(7)	
27	Det.6	17.8(9)	2.1(7)	7.8(7)	80.2(20)	2.8(6)					30.1(11)	
28	Det.6	16.6(9)		7.6(7)	78.3(19)	3.2(6)	1.8(6)				30.8(12)	
29	Det.6	17.1(7)	2.2(6)	7.2(6)	79.0(17)	2.8(5)	1.5(5)				29.5(10)	
30	Det.6	17.0(6)	2.6(4)	8.5(5)	80.1(16)	2.4(3)	2.1(3)				28.8(8)	
31	Det.6	16.6(4)	2.62(26)	8.86(29)	78.4(14)	2.82(19)	1.85(20)			0.78(15)	29.5(6)	0.38(10)
32	Det.7	14(4)			87(8)						30(5)	
33	Det.5	16.6(5)	2.91(29)	8.4(3)	77.4(15)	2.57(25)	1.67(25)	0.84(22)		0.65(16)	29.8(8)	
34	Det.7	16.9(3)	3.08(9)	9.21(21)	78.9(16)	2.76(9)	1.87(7)	0.62(6)		0.67(5)	28.0(5)	0.36(3)
35	Det.13				79.8(23)							
36	Det.10				83.3(16)							
37	Det.13				79.2(21)							
38	Det.10				81.8(15)							
39	Det.13				77.7(16)							
40	Det.10				79.6(15)							
41	Det.13				79.0(17)							
42	Det.10				80.0(16)							
43	Det.13				80.2(22)							
44	Det.10				80.6(18)							
45	Det.17	18.4(23)			80(3)						28.0(24)	
46	Det.17	16.0(19)			82(3)						32.8(23)	
47	Det.17	18.8(18)		8.3(13)	74.8(26)						30.3(20)	
48	Det.17	19.5(18)		9.7(15)	78(3)						26.8(22)	
49	Det.17	15.8(18)		11.6(20)	82(3)						28.5(20)	
50	Det.19	20.4(12)			80.6(26)						25.3(18)	
51	Det.17	13.6(15)		7.9(11)	77(3)						29.7(23)	
52	Det.17	18.5(14)		8.9(13)	79(3)						31.5(18)	
53	Det.17	16.1(15)		9.4(13)	82.1(29)						35.3(24)	
54	Det.17	12.4(12)		7.9(10)	79.0(29)						27.6(18)	
55	Det.17	17.1(18)		10.5(14)	82(3)						25.8(20)	
56	Det.19	15.6(10)			76.7(21)						28.2(18)	
57	Det.17	21.4(19)		8.2(11)	80(3)						25.3(19)	
58	Det.17	15.6(14)		9.7(11)	75.7(26)						26.7(18)	
59	Det.17	14.7(14)		5.8(10)	76.3(26)						27.7(16)	
60	Det.17	16.6(14)		8.1(11)	83.5(28)						27.7(16)	
61	Det.17	17.3(15)		8.7(11)	79.2(28)						30.9(17)	
62	Det.19	17.9(15)			82.1(29)						25.1(21)	
63	Det.17	20.6(18)		9.3(10)	80.6(27)						28.8(19)	
64	Det.17	16.4(16)		9.2(10)	78.3(25)						30.2(17)	
65	Det.17	18.6(17)		7.8(10)	75.3(27)						30.6(17)	
66	Det.17	14.5(14)		10.7(10)	80.0(28)						28.7(20)	
67	Det.17	19.1(13)		10.4(14)	77.0(27)						31.3(19)	
68	Det.19	12.8(13)			75.0(26)						29.3(28)	

(*continued on next page*)

Table 5 (*continued*).

#	Det.	E_γ (keV)										
		373.050	529.169	588.605	656.008	816.692	841.211	902.294	1099.560	1132.351	1185.234	1446.492
69	Det.18	16.2(12)		8.4(7)	78.0(24)						26.8(13)	
70	Det.18	20.5(13)		10.3(10)	78.9(25)						28.1(16)	
71	Det.18	15.1(8)		8.1(8)	76.5(23)						26.6(12)	
72	Det.18	16.9(9)		9.3(7)	77.0(24)						26.1(13)	
73	Det.18	18.7(11)		9.4(9)	79.2(25)						27.8(13)	
74	Det.19	15.0(15)			76.8(29)						24(3)	
75	Det.18	16.4(11)		9.1(8)	82.0(24)						31.9(14)	
76	Det.18	18.0(10)		8.2(8)	79.5(24)						28.1(13)	
77	Det.18	16.1(8)		9.7(9)	81.3(23)						30.0(14)	
78	Det.18	17.6(9)		8.8(7)	81.8(22)						28.7(12)	
79	Det.18	18.4(10)		7.9(7)	79.7(23)						29.0(14)	
80	Det.19	16.7(21)			77(3)						26.2(28)	
81	Det.18	16.2(9)		9.3(7)	81.2(22)						29.3(12)	
82	Det.18	16.5(11)		7.9(7)	79.5(23)						29.4(20)	
83	Det.18	18.4(10)		9.5(6)	78.6(22)						26.8(12)	
84	Det.18	15.7(7)		9.3(7)	76.7(21)						27.7(13)	
85	Det.18	15.0(7)		7.9(6)	77.0(21)						29.3(14)	
86	Det.19	18.1(18)			78(3)						32(4)	
87	Det.18	18.6(8)		8.3(6)	78.8(23)						27.6(12)	
88	Det.18	17.4(10)		9.1(6)	77.5(21)						27.1(12)	
89	Det.18	18.8(10)		9.1(5)	81.5(21)						30.6(12)	
90	Det.18	15.6(7)		9.4(6)	77.8(22)						27.6(13)	
91	Det.18	16.7(8)		7.9(6)	77.6(22)						28.0(12)	
92	Det.19	23.4(24)			83(4)						32(3)	
93	Det.18	17.2(8)		9.5(6)	80.4(22)						28.4(11)	
94	Det.18	16.7(9)		7.9(6)	77.8(21)						26.5(11)	
95	Det.18	17.7(8)		9.0(5)	77.4(21)						27.5(12)	
96	Det.18	16.6(8)		9.3(6)	79.0(21)						28.9(12)	
97	Det.18	17.1(8)		8.4(5)	82.0(21)						26.8(11)	
98	Det.19	19.5(25)			68(3)						27(4)	
99	Det.18	15.1(9)		8.8(5)	78.0(21)						28.6(11)	
100	Det.18	16.4(8)		8.2(5)	78.9(22)						28.2(13)	
101	Det.18	16.5(8)		9.3(6)	75.4(21)						29.6(11)	
102	Det.18	17.5(9)		8.9(6)	80.5(21)						27.4(11)	
103	Det.18	18.2(7)		9.4(6)	79.6(22)						28.6(11)	
104	Det.19				74(4)							
105	Det.12	17.1(5)	3.36(23)	9.0(3)	79.8(14)	2.59(21)	1.80(18)	0.51(16)	2.12(18)	0.86(15)	28.9(6)	0.46(10)
106	Det.12	16.8(5)	3.40(28)	9.1(4)	78.7(15)	2.90(27)	1.92(22)		1.93(22)	1.15(20)	29.4(7)	
107	Det.12	16.7(6)	3.4(3)	9.2(4)	78.6(16)	2.15(28)	1.60(24)		2.18(24)	0.98(19)	29.4(8)	
Wgt. Mean		16.87(22)	3.03(7)	8.82(13)	79.3(10)	2.67(6)	1.88(5)	0.63(6)	2.16(12)	0.73(4)	28.8(4)	0.37(3)
χ^2/ν		1.76	0.89	1.32	1.25	0.74	0.88	0.63	1.15	1.77	1.46	0.44
NDS		17.6(4)	3.10(10)	9.57(17)	88.3(15)	2.52(6)	1.75(5)	0.68(4)	2.01(5)	0.74(3)	30.7(6)	0.370(20)
ENSDF2020		16.8(4)	2.92(7)	9.16(10)	82(14)	2.76(7)	1.87(7)	0.681(20)	2.11(7)	0.71(3)	28.6(6)	0.36(20)

to contribute a small fraction (~10%) to a small effect (~1%) and neglected.

Coincidence summing was expected to be most significant in the counting geometry designated Det.19 in Exp.7 since the foils were placed only 5.2 cm from the front face of the detector. For all other cases, activation foils were placed far enough away (> 12 cm) that the effect was not expected to be significant. In fact, the effect on both the ^{152}Eu calibration and ^{61}Cu photopeaks was calculated to be on order of 0.1% or less for every configuration but Det.19 and therefore neglected.

For Det.19, Fig. 6 illustrates that the effect on the ratio of efficiencies generated from ^{152}Eu, relative to 283 keV, was found to be on order of only ~1%. The detection of 656 keV γ rays from ^{61}Cu increases by 1% (while the detection of 283 keV and 373 keV γ rays decreases by, respectively, 1.2% and 5.8%. This results in a net decrease in the observed 656/283 intensity ratio of 2.2% and increase of the 373/283 intensity ratio of 4.6%. Other observed transitions were unaffected. In addition to making these coincident summing adjustments, an additional 1% uncertainty was applied to the Det.19 measurements to account for the inexactness of these methods and the potential angular distribution effects.

3. Results

As previously noted, the accepted ratio of 656 keV γ-ray intensity to that of 283 keV in ^{61}Cu from the NDS is 88.3(15)%. Our 107 measured ratios are plotted in Fig. 7, showing a clear deviation from this value. The weighted mean of this ratio is 0.794 with 0.001 statistical uncertainty (1σ) and 0.010 systematic. Removing the LANL (Exp. 3, brown diamonds) data from the calculation (because the measurements and calibration procedure were performed by another group) and/or those counted close to the detector (Det.19, open green circles), did not change this mean or its uncertainty. This mean is 10% (>5σ) lower than the NDS value.

A complete listing of the intensities, relative to the 283 keV emission, of all γ rays detected with significant strength is tabulated in Table 5. Although the 67 keV emission was usually quite strong, it has been excluded due to the inaccuracy of extrapolating the ^{152}Eu-generated efficiency calibration below 121 keV. Also excluded was the 909 keV emission as there is a known doublet with a 909.2 keV γ-ray from competing reactions producing ^{60}Cu (e.g. from (d,2n) reactions on ^{60}Ni), which decays with a half life of 23.7 min. Both statistical and systematic uncertainties are included, but only statistical sources (from counting/peak fitting and efficiency fit variability) are used in the calculation of the weighted mean and reduced χ^2. Due to the large number of datapoints, the uncertainty in the mean is dominated by systematic sources (primarily, the 1.24% efficiency interpolation uncertainty).

For most energies when sufficient datapoints were measured, the reduced χ^2 is above unity, indicating slightly more statistical variation than is reflected by our uncertainty assessment. Factoring in an additional 1% statistical uncertainty for the 656 keV values, for instance,

Table 6
Ratios of γ-ray intensities, in percent, at energy E_γ relative to the intensity at 656 keV. NDS (Zuber and Singh, 2015) and the recent 2020 ENSDF re-evaluation (ENSDF, 2020) values are included for comparison with the weighted means as well as the reduced χ^2 of the data from this mean. The 17% uncertainty in the normalization emission (656 keV) indicated in the ENSDF re-evaluation was not incorporated into the other γ-ray energy's intensity uncertainties. All measurements' uncertainties reflect counting/peak fitting and "fit variability" uncertainties, each considered statistical and used solely in the calculation of the weighted mean and reduced χ^2, as well as a 1.24% "efficiency interpolation" uncertainty, which was treated as systematic and added in quadrature to the final weighted mean uncertainty.

f#	Det.	E_γ (keV)										
		282.956	373.050	529.169	588.605	816.692	841.211	902.294	1099.560	1132.351	1185.234	1446.492
1	Det.1	131(4)	21.8(12)	4.1(7)	10.7(9)	3.3(7)	2.4(7)				40.1(18)	
2	Det.1	126(3)	19.3(12)	3.6(6)	11.3(9)	3.1(6)	3.3(6)		3.0(7)		37.0(19)	
3	Det.1	128(4)	22.7(15)	3.3(8)	10.5(11)	4.1(8)	2.6(8)		4.8(10)		38.4(21)	
4	Det.1	122.4(28)	19.2(10)	3.6(6)	12.3(8)	2.9(6)	3.7(7)		3.5(9)		37.5(15)	
5	Det.2	129(5)	22.9(20)		10.7(16)	4.1(12)					36(3)	
6	Det.2	125(3)	20.2(9)	3.3(8)	9.0(8)	2.1(8)					37.9(15)	
7	Det.2	126(3)	19.7(13)	4.3(10)	10.9(10)	2.5(9)					40.4(21)	
8	Det.4	124.5(20)	21.3(7)	3.5(4)	11.6(4)	3.1(5)	3.1(4)		3.4(9)		36.3(11)	
9	Det.9	124.6(21)	20.8(7)		11.7(6)						36.3(10)	
10	Det.9	123(3)	20.9(17)		11.4(14)						36.1(21)	
11	Det.9	130(8)									34(4)	
12	Det.9	121.5(27)	22.8(13)		8.7(10)						39.8(17)	
13	Det.9	134(6)	18(3)								31(4)	
14	Det.9	142(17)										
15	Det.9	131(3)	23.4(14)		9.5(11)						36.0(18)	
16	Det.9	122(6)	23(4)		14.0(29)						31(4)	
17	Det.9	120.3(29)	20.2(14)		8.8(11)						31.7(17)	
18	Det.9	125(7)	29(4)								43(5)	
19	Det.9	125(4)	20.4(18)		9.6(16)						38.1(25)	
20	Det.9	121(4)	19.6(24)								35(3)	
21	Det.5	128(5)	18.7(22)		12.0(20)						36(4)	
22	Det.5	119(5)	20.3(21)		10.7(20)						35(4)	
23	Det.5	118(5)	19.2(24)		10.3(23)						39(4)	
24	Det.8	126.6(28)	22.0(6)	3.8(3)	11.5(4)	3.1(3)	2.3(4)	1.0(3)			35.8(10)	
25	Det.5	142(7)	24.3(28)		10.3(26)						38(4)	
26	Det.7	125.9(28)	21.7(5)	3.71(26)	11.0(4)	3.34(29)	2.6(3)				37.3(10)	
27	Det.6	125(3)	22.2(11)	2.6(9)	9.8(9)	3.5(8)					37.6(15)	
28	Det.6	128(3)	21.2(12)		9.7(9)	4.0(8)	2.3(8)				39.4(16)	
29	Det.6	126.5(29)	21.7(9)	2.8(7)	9.1(7)	3.5(6)	1.9(7)				37.3(13)	
30	Det.6	124.8(26)	21.3(7)	3.2(6)	10.6(6)	2.9(4)	2.6(4)				35.9(10)	
31	Det.6	127.6(22)	21.2(5)	3.4(3)	11.3(4)	3.59(24)	2.36(25)			1.00(19)	37.6(8)	0.48(13)
32	Det.7	115(8)	16(5)								34(6)	
33	Det.5	129.2(24)	21.4(7)	3.8(4)	10.8(5)	3.3(3)	2.2(3)	1.09(28)		0.84(21)	38.5(10)	
34	Det.7	126.8(26)	21.4(4)	3.91(10)	11.67(19)	3.50(10)	2.37(8)	0.78(8)		0.85(6)	35.5(7)	0.46(4)
35	Det.13	125(4)										
36	Det.10	120.0(24)										
37	Det.13	126(3)										
38	Det.10	122.3(25)										
39	Det.13	128.7(28)										
40	Det.10	125.6(24)										
41	Det.13	126.6(28)										
42	Det.10	125.0(25)										
43	Det.13	125(4)										
44	Det.10	124.0(29)										
45	Det.17	126(6)	23(3)								35(3)	
46	Det.17	122(5)	19.5(23)								39.9(29)	
47	Det.17	134(4)	25.1(24)		11.1(18)						40.5(28)	
48	Det.17	128(6)	24.9(24)		12.4(20)						34.1(29)	
49	Det.17	122(4)	19.2(22)		14.1(25)						34.7(25)	
50	Det.19	124(4)	25.3(15)								31.4(23)	
51	Det.17	130(6)	17.6(20)		10.3(14)						39(3)	
52	Det.17	127(5)	23.5(19)		11.3(16)						40.0(24)	
53	Det.17	122(4)	19.6(18)		11.4(16)						43(3)	
54	Det.17	127(5)	15.7(16)		10.0(12)						35.0(24)	
55	Det.17	123(4)	21.0(22)		12.8(17)						31.6(25)	
56	Det.19	130(3)	20.4(14)								36.8(24)	
57	Det.17	125(5)	26.8(25)		10.3(14)						31.8(24)	
58	Det.17	132(5)	20.6(19)		12.8(14)						35.2(25)	
59	Det.17	131(4)	19.3(19)		7.5(13)						36.3(22)	
60	Det.17	120(4)	19.9(17)		9.7(13)						33.1(20)	
61	Det.17	126(4)	21.8(19)		10.9(14)						39.0(23)	
62	Det.19	122(4)	21.8(19)								30.6(26)	
63	Det.17	124(4)	25.5(23)		11.6(13)						35.8(24)	
64	Det.17	128(4)	21.0(20)		11.8(12)						38.6(23)	
65	Det.17	133(5)	24.7(22)		10.4(13)						40.6(23)	
66	Det.17	125(4)	18.2(17)		13.4(13)						35.9(25)	
67	Det.17	130(5)	24.7(17)		13.6(18)						40.6(25)	
68	Det.19	133(4)	17.1(18)								39(4)	

(*continued on next page*)

Table 6 (*continued*).

f#	Det.	E_γ (keV)										
		282.956	373.050	529.169	588.605	816.692	841.211	902.294	1099.560	1132.351	1185.234	1446.492
69	Det.18	128(4)	20.7(15)		10.8(9)						34.4(18)	
70	Det.18	127(4)	26.0(16)		13.1(12)						35.6(20)	
71	Det.18	131(4)	19.8(10)		10.6(10)						34.7(16)	
72	Det.18	130(4)	21.9(13)		12.1(9)						33.9(17)	
73	Det.18	126(4)	23.6(14)		11.9(11)						35.1(17)	
74	Det.19	130(5)	19.6(20)								32(4)	
75	Det.18	122(3)	20.1(14)		11.1(10)						38.9(17)	
76	Det.18	126(3)	22.6(13)		10.3(10)						35.3(17)	
77	Det.18	123(3)	19.8(10)		12.0(11)						36.8(18)	
78	Det.18	122.3(29)	21.5(11)		10.8(8)						35.1(15)	
79	Det.18	126(3)	23.1(13)		10.0(9)						36.3(18)	
80	Det.19	130(5)	21.7(27)								34(4)	
81	Det.18	123(3)	19.9(11)		11.4(8)						36.1(16)	
82	Det.18	126(4)	20.7(14)		10.0(8)						37.0(25)	
83	Det.18	127(3)	23.4(13)		12.1(8)						34.1(15)	
84	Det.18	130(3)	20.5(9)		12.1(9)						36.1(17)	
85	Det.18	130(3)	19.5(10)		10.2(8)						38.1(19)	
86	Det.19	128(5)	23.2(24)								41(5)	
87	Det.18	127(4)	23.6(11)		10.5(8)						35.0(15)	
88	Det.18	129(3)	22.5(13)		11.7(8)						35.0(16)	
89	Det.18	122.8(29)	23.0(12)		11.2(7)						37.6(15)	
90	Det.18	128(3)	20.1(10)		12.1(8)						35.5(17)	
91	Det.18	129(3)	21.5(10)		10.2(8)						36.0(15)	
92	Det.19	120(6)	28(3)								38(4)	
93	Det.18	124(3)	21.4(10)		11.8(8)						35.3(14)	
94	Det.18	129(3)	21.4(11)		10.2(7)						34.1(14)	
95	Det.18	129(3)	22.9(10)		11.6(7)						35.5(16)	
96	Det.18	127(3)	21.0(10)		11.8(8)						36.6(15)	
97	Det.18	122(3)	20.8(10)		10.2(6)						32.7(13)	
98	Det.19	147(8)	29(4)								40(6)	
99	Det.18	128(4)	19.3(11)		11.3(7)						36.7(15)	
100	Det.18	127(3)	20.8(11)		10.3(6)						35.8(17)	
101	Det.18	133(3)	21.9(11)		12.3(8)						39.2(15)	
102	Det.18	124.3(29)	21.7(11)		11.1(7)						34.1(14)	
103	Det.18	126(3)	22.9(9)		11.9(7)						36.0(15)	
104	Det.19	135(7)										
105	Det.12	125.3(22)	21.4(6)	4.21(29)	11.3(4)	3.25(26)	2.25(22)	0.64(20)	2.65(23)	1.07(19)	36.3(8)	0.58(13)
106	Det.12	127.0(24)	21.3(7)	4.3(4)	11.5(4)	3.7(3)	2.44(28)		2.46(28)	1.46(25)	37.4(10)	
107	Det.12	127.2(25)	21.2(7)	4.3(4)	11.7(5)	2.7(4)	2.0(3)		2.8(3)	1.25(25)	37.3(10)	
Wgt. Mean		125.9(16)	21.36(28)	3.85(8)	11.28(16)	3.40(8)	2.38(7)	0.79(7)	2.73(15)	0.92(5)	36.4(5)	0.47(4)
χ^2/ν		1.22	1.63	0.93	1.41	0.81	0.81	0.69	1.12	1.74	1.41	0.40
NDS		113.3(17)	19.9(5)	3.51(11)	10.84(19)	2.85(7)	1.98(6)	0.77(5)	2.28(6)	0.83(4)	34.8(7)	0.419(23)
ENSDF2020		122(5)	20.5(5)	3.56(8)	11.18(12)	3.37(8)	2.28(9)	0.831(24)	2.57(8)	0.87(4)	34.9(7)	0.44(24)

would make the reduced χ^2 unity, while as much as 5% would need to be added to the 373 keV values. This would only change those weighted means to, respectively, 79.3(10)% and 16.77(26)%, well within the calculated uncertainties, still dominated by systematics.

The same intensity data, normalized to the secondary 656 keV γ ray instead of 283 keV, is tabulated in Table 6. The agreement of all twelve of these ratios with the NDS is considerably and systematically worse than those in Table 5, which agree within 1σ uncertainty in all but three cases. This convincingly suggests that the most probable error in the NDS is in the 656 keV intensity rather than that of 283 keV. Assuming no change in the 12.2% intensity of this emission, the 656 keV intensity would then be 9.69(12)% with relative uncertainty, or 9.7(17)% including the overall 18% absolute γ-branch uncertainty.

Comparison with the 2020 ENSDF re-evaluation is much better at all energies. Agreement is also more independent of the normalization chosen than the NDS, due to the improved 656/283 keV intensity ratio. The intensities at 588 keV and 1185 keV in particular also appear to have been dramatically improved over the NDS values, where they differ from our observations by more than 2σ.

Plots of all the 283 keV-normalized ratios are shown in Fig. 8.

4. Conclusions

Through a large number of activation measurements, there is overwhelming evidence for significant nuclear data errors in the ratio of primary-to-secondary γ ray emissions of ^{61}Cu and a correction to the NDS is recommended. Though we were not able to definitively measure the absolute intensities of each γ ray, agreement with eleven other emissions suggests the error lies with the 656 keV intensity which should accordingly be adjusted to 79.3(10)% of relative γ-branch ^{61}Cu decays and 9.7(17)% of absolute decays. A recent re-evaluation in the ENSDF database incorporated multiple, but older and widely-discrepant, measurements. Our measurements compare much more favorably with this re-evaluation but provide an order-of-magnitude improvement to the relative uncertainty of the 656 keV emission intensity.

This error has wide implications for its recommended use as a proton and deuteron beam current monitor and any cross sections measured in ratio to such reactions. Ambiguities in the methodologies for past measurements of the ^{nat}Ni(d,x)^{61}Cu reaction make the precise impacts unpredictable. However, as evidence suggests that much of the experimental data used for the evaluation of this cross section was normalized either solely to the 656 keV γ ray or to a weighted average with the primary, a re-evaluation of this cross section, and any cross sections measured in ratio to it, may be necessary.

We were not able to determine the absolute intensity of any γ-ray or the overall gamma branch, versus β^+ or electron capture directly to the ground state, per decay of ^{61}Cu. The uncertainty in this value, reported as 18% in the NDS and 15% in the ENSDF re-evaluation, is considerable. However, the cross sections of reactions such as ^{nat}Ni(d,x)^{61}Cu

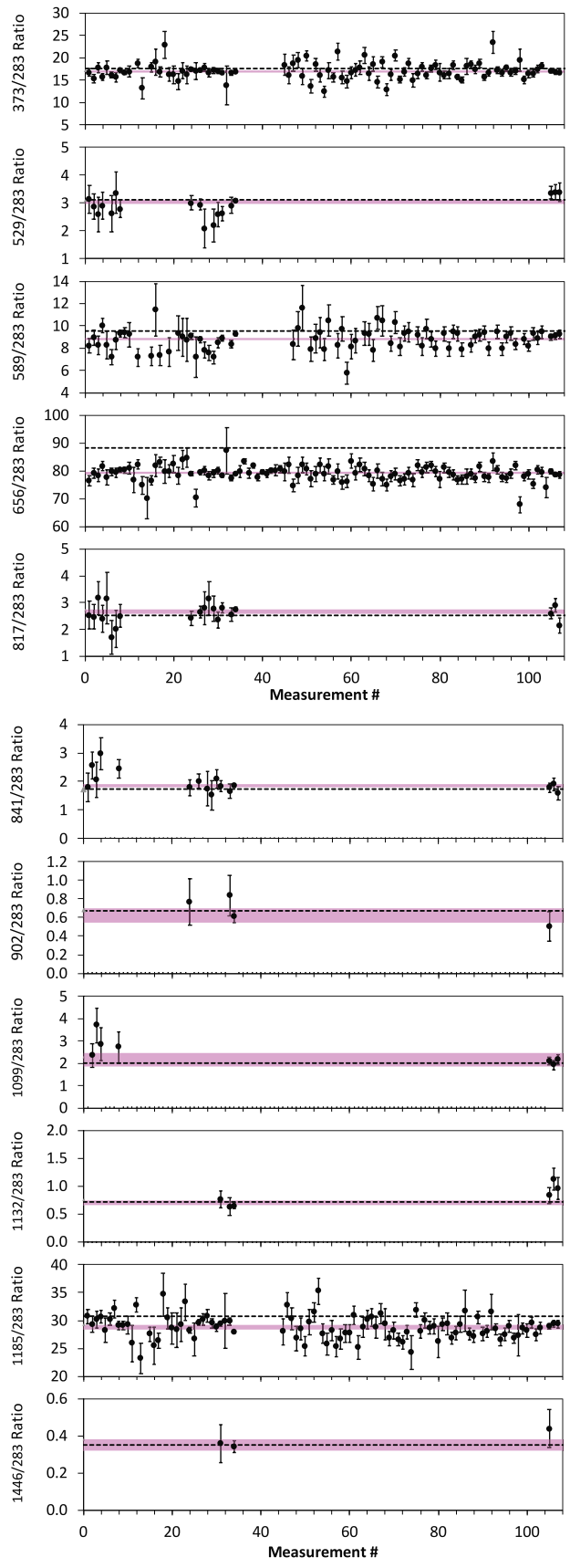

Fig. 8. (Color online) All γ-ray intensity measurements from ^{61}Cu decay in ratio to the 283 keV γ ray emission, expressed in percent. Error bars show statistical counting uncertainty only. Dashed lines indicate the Nuclear Data Sheets value while magenta bands represent weighted mean of measured data, with band thickness showing weighted statistical uncertainty.

may be measured with a specific characteristic γ-ray tag and if the same energy γ-ray is used in subsequent monitor activation reactions, this absolute uncertainty can be neglected. Unfortunately, as previously noted, many cross section measurements have been somewhat ambiguous as to the specific γ-ray energies used in their generation. Furthermore, in most contributions to this evaluated ^{nat}Ni(d,x)^{61}Cu cross section (Hermanne et al., 2018), a complete uncertainty budget was not provided. However, the fact that most measurements report uncertainties lower than this gamma branch uncertainty (e.g. ~12% from Takács et al. (2007)) appears to indicate that this contribution was neglected. If true, the cross section uncertainties should be added in quadrature to the gamma branch uncertainty when calculating the true number of ^{61}Cu atoms produced.

Although the gamma branch uncertainty may be neglected when activation products are used for beam monitoring, future studies are recommended to determine the absolute intensity of one or more of the most intense γ rays through β^+-particle detection or observation of the 511 keV pair-production γ ray. The latter would require careful background subtraction, precise half-life fitting of multiple time-dependent measurements. In either case, low production irradiation energies are needed to minimize contributions from competing β^+-emitting reaction products. The electron capture contribution would then need to be measured through X-ray detection or, as is currently the case, reliance on theoretical ϵ/β^+ values.

Declaration of competing interest

The authors declare that they have no known competing financial interests or personal relationships that could have appeared to influence the work reported in this paper.

Acknowledgments

We would like to thank the operations staff of the 88-Inch Cyclotron at Lawrence Berkeley National Laboratory and both the Isotope Production Facility and the Nuclear and Radiochemistry Countroom at Los Alamos National Laboratory for their support. We also acknowledge and thank the myriad students, postdocs, and staff who supported the original measurements from which this data was culled. This work was performed under the auspices the U.S. Department of Energy by Lawrence Livermore National Laboratory under Contract DE-AC52-07NA27344 and Lawrence Berkeley National Laboratory under Contract No. DE-AC02-05CH11231. This research is supported by the U.S. Department of Energy Isotope Program, managed by the Office of Science for Nuclear Physics. The primary sponsor of the first author is U.S. Department of Energy by Lawrence Livermore National Laboratory under Contract DE-AC52-07NA27344.

References

Aslam, M.N., Qaim, S.M., 2014a. Nuclear model analysis of excitation functions of proton and deuteron induced reactions on ^{64}Zn and ^{3}He- and α-particle induced reactions on ^{59}Co leading to the formation of copper-61: Comparison of major production routes. Appl. Radiat. Isot. 94, 131–140. http://dx.doi.org/10.1016/j.apradiso.2014.08.001.

Aslam, M.N., Qaim, S.M., 2014b. Nuclear model analysis of excitation functions of proton, deuteron and α-particle induced reactions on nickel isotopes for production of the medically interesting copper-61. Appl. Radiat. Isot. 89, 65–73. http://dx.doi.org/10.1016/j.apradiso.2014.02.007.

Béraud, R., Berkes, I., Daniére, J., Lévy, M., Marest, G., Rougny, R., 1967. Sur les niveaux excités du ^{61}Ni. Nuclear Phys. A 99 (4), 577–584. http://dx.doi.org/10.1016/0375-9474(67)90372-7.

Bolotin, H.H., Fischbeck, H.J., 1967. Decay of Cu^{61} and Energy Levels in Ni^{61}. Phys. Rev. 158, 1069–1072. http://dx.doi.org/10.1103/PhysRev.158.1069.

Brune, C.R., Kavanagh, R.W., Rolfs, C., 1994. ^{3}H(α,γ)^{7}Li reaction at low energies. Phys. Rev. C 50, 2205–2218. http://dx.doi.org/10.1103/PhysRevC.50.2205.

Coetzee, P.A., Peisach, M., 1972. Activation cross sections for deuteron-induced reactions on some elements of the first transition series, up to 5.5 MeV. Radiochim. Acta 17 (1), 1–6. http://dx.doi.org/10.1524/ract.1972.17.1.1.

Cogneau, M., Gilly, L.J., Cara, J., 1967. Absolute cross sections and excitation functions for deuteron-induced reactions on the nickel isotopes between 2 and 12 MeV. Nuclear Phys. A 99 (4), 686–694. http://dx.doi.org/10.1016/0375-9474(67)90379-X.

Cvetinović, A., Likar, A., Lipoglavšek, M., Mihelič, A., Petrovič, T., Vesić, J., Vodenik, B., 2015. Precise measurement of the half-life of ^{61}Cu. Appl. Radiat. Isot. 104, 160–166. http://dx.doi.org/10.1016/j.apradiso.2015.07.005.

Ekeberg, H., 2020. Nuclear Excitation Functions For Medical Isotope Production: Targeted Radionuclide Therapy via ^{Nat}Ir(d,x)^{193m}Pt (Master's thesis). University of Oslo, URL: https://www.duo.uio.no/bitstream/handle/10852/79795/1/Masterthesis_Ekeberg.pdf.

ENSDF, 2020. ENSDF document available from the National Nuclear Data Center ^{61}Cu EC Decay dataset. URL: www.nndc.bnl.gov/ensdf/.

Fitzpeaks, 2014. URL: http://www.jimfitz.co.uk/fitzpeak.htm.

Garrido, E., Duchemin, C., Guertin, A., Haddad, F., Michel, N., Métivier, V., 2016. New excitation functions for proton induced reactions on natural titanium, nickel and copper up to 70MeV. Nucl. Instrum. Methods Phys. Res. B 383, 191–212. http://dx.doi.org/10.1016/j.nimb.2016.07.011.

Graves, S.A., Ellison, P.A., Barnhart, T.E., Valdovinos, H.F., Birnbaum, E.R., Nortier, F.M., Nickles, R.J., Engle, J.W., 2016. Nuclear excitation functions of proton-induced reactions (Ep=35–90MeV) from Fe, Cu, and Al. Nucl. Instrum. Methods Phys. Res. B 386, 44–53. http://dx.doi.org/10.1016/j.nimb.2016.09.018.

Grütter, A., 1982. Decay data of $^{55-58}$Co, ^{57}Ni, ^{60,61}Cu and ^{62,63}Zn. Int. J. Appl. Radiat. Isot. 33 (7), 533–535. http://dx.doi.org/10.1016/0020-708X(82)90008-4.

Gyürky, G., Halász, Z., Kiss, G.G., Szücs, T., Fülöp, Z., 2019. Half-life measurement of ^{65}Ga with γ-spectroscopy. Appl. Radiat. Isot. 148, 87–90. http://dx.doi.org/10.1016/j.apradiso.2019.03.021.

Hermanne, A., Ignatyuk, A., Capote, R., Carlson, B., Engle, J., Kellett, M., Kibédi, T., Kim, G., Kondev, F., Hussain, M., Lebeda, O., Luca, A., Nagai, Y., Naik, H., Nichols, A., Nortier, F., Suryanarayana, S., Takács, S., Tárkányi, F.T., Verpelli, M., 2018. Reference cross sections for charged-particle monitor reactions. Nucl. Data Sheets 148, 338–382, (Special Issue on Nuclear Reaction Data). http://dx.doi.org/10.1016/j.nds.2018.02.009.

Kireeff Covo, M., Albright, R.A., Ninemire, B.F., Johnson, M.B., Hodgkinson, A., Loew, T., Benitez, J.Y., Todd, D.S., Xie, D.Z., Perry, T., Phair, L., Bernstein, L.A., Bevins, J., Brown, J.A., Goldblum, B.L., Harasty, M., Harrig, K.P., Laplace, T.A., Matthews, E.F., Bushmaker, A., Walker, D., Oklejas, V., Hopkins, A.R., Bleuel, D.L., Chen, J., Cronin, S.B., 2018. The 88-Inch Cyclotron: A one-stop facility for electronics radiation and detector testing. Measurement 127, 580–587. http://dx.doi.org/10.1016/j.measurement.2017.10.018.

McCarthy, D.W., Bass, L.A., Cutler, P.D., Shefer, R.E., Klinkowstein, R.E., Herrero, P., Lewis, J.S., Cutler, C.S., Anderson, C.J., Welch, M.J., 1999. High purity production and potential applications of copper-60 and copper-61. Nucl. Med. Biol. 26 (4), 351–358. http://dx.doi.org/10.1016/S0969-8051(98)00113-9.

Meyer, R.A., Prindle, A.L., Myers, W.A., Hopke, P.K., Dieterly, D., Koops, J.E., 1978. Multiparticle configurations in the odd-neutron nuclei ^{61}Ni and ^{67}Zn populated by decay of ^{61}Cu, ^{67}Cu, and ^{67}Ga. Phys. Rev. C 17, 1822–1831. http://dx.doi.org/10.1103/PhysRevC.17.1822.

Morrell, J.T., Voyles, A.S., Basunia, M.S., Batchelder, J.C., Matthews, E.F., Bernstein, L.A., 2020. Measurement of ^{139}La(p,x) cross sections from 35–60 MeV by stacked-target activation. Eur. Phys. J. A 56 (1), 13. http://dx.doi.org/10.1140/epja/s10050-019-00010-0.

Nelson, N., Ellison, P., Nickles, R., McCutchan, E., Sonzogni, A., Smith, S., Greene, J., Carpenter, M., Zhu, S., Lister, C., Moran, K., 2017. High-precision gamma-ray spectroscopy of ^{61}Cu, an emerging medical isotope used in positron emission tomography. In: Poster presented at the 2017 Fall Meeting of the APS Division of Nuclear Physics. URL: http://meetings.aps.org/link/BAPS.2017.DNP.EA.180.

Qaim, S.M., 2019. Theranostic radionuclides: recent advances in production methodologies. J. Radioanal. Nucl. Chem. 322 (3), 1257–1266. http://dx.doi.org/10.1007/s10967-019-06797-y.

Ritter, J.C., Larson, R.E., 1969. Decay of ^{61}Cu; Energy levels of ^{61}Ni. Nuclear Phys. A 127 (2), 399–411. http://dx.doi.org/10.1016/0375-9474(69)90580-6.

Ruangma, A., Bai, B., Lewis, J.S., Sun, X., Welch, M.J., Leahy, R., Laforest, R., 2006. Three-dimensional maximum a posteriori (MAP) imaging with radiopharmaceuticals labeled with three Cu radionuclides. Nucl. Med. Biol. 33 (2), 217–226. http://dx.doi.org/10.1016/j.nucmedbio.2005.11.001, URL: http://www.sciencedirect.com/science/article/pii/S0969805105002763.

Satyanarayana, G., Venkateswara Rao, N., Sri Krishna, G.S., Chandrasekhar Rao, M.V.S., Reddy, S.B., Sastry, D.L., Chinthalapudi, S.N., Rao, V.V., 1988. Decay of ^{61}Cu. Il Nuovo Cimento A (1971-1996) 99 (3), 309–315. http://dx.doi.org/10.1007/BF02733823.

Schöneberg, R., Flammersfeld, A., 1967. Der Zerfall des Cu61. Z. Phys. 200 (2), 205–212. http://dx.doi.org/10.1007/BF01328935.

Semkow, T.M., Mehmood, G., Parekh, P.P., Virgil, M., 1990. Coincidence summing in gamma-ray spectroscopy. Nucl. Instrum. Methods Phys. Res. A 290 (2), 437–444. http://dx.doi.org/10.1016/0168-9002(90)90561-J.

Shahid, M., Kim, K., Naik, H., Zaman, M., Yang, S.-C., Kim, G., 2015. Measurement of excitation functions in proton induced reactions on natural copper from their threshold to 43MeV. Nucl. Instrum. Methods Phys. Res. B 342, 305–313. http://dx.doi.org/10.1016/j.nimb.2014.10.019.

Singh, B., 2019. Personal communication.

Takács, S., 2020. Personal communication.

Takács, S., Sonck, M., Azzam, A., Hermanne, A., Tárkányi, F., 1997. Activation cross section measurements of deuteron induced reactions on nat Ni with special reference to beam monitoring and production of for ^{61}Cu medical purpose. Radiochim. Acta 76 (1–2), 15–24. http://dx.doi.org/10.1524/ract.1997.76.12.15.

Takács, S., Szelecsényi, F., Tárkányi, F., Sonck, M., Hermanne, A., Shubin, Y., Dityuk, A., Mustafa, M.G., Youxiang, Z., 2001. New cross-sections and intercomparison of deuteron monitor reactions on Al, Ti, Fe, Ni and Cu. Nucl. Instrum. Methods Phys. Res. B 174 (3), 235–258. http://dx.doi.org/10.1016/S0168-583X(00)00589-9.

Takács, S., Tárkányi, F., Király, B., Hermanne, A., Sonck, M., 2007. Evaluated activation cross sections of longer-lived radionuclides produced by deuteron induced reactions on natural nickel. Nucl. Instrum. Methods Phys. Res. B 260 (2), 495–507. http://dx.doi.org/10.1016/j.nimb.2006.11.136.

Červenák, J., Lebeda, O., 2020. New cross-section data for proton-induced reactions on natTi and natCu with special regard to the beam monitoring. Nucl. Instrum. Methods Phys. Res. B 480, 78–97. http://dx.doi.org/10.1016/j.nimb.2020.08.006.

Voyles, A.S., Bernstein, L.A., Birnbaum, E.R., Engle, J.W., Graves, S.A., Kawano, T., Lewis, A.M., Nortier, F.M., 2018. Excitation functions for (p,x) reactions of niobium in the energy range of Ep = 40–90 MeV. Nucl. Instrum. Methods Phys. Res. B 429, 53–74. http://dx.doi.org/10.1016/j.nimb.2018.05.028.

Voyles, A.S., Lewis, A.M., Morrell, J.T., Basunia, M.S., Bernstein, L.A., Engle, J.W., Graves, S.A., Matthews, E.F., 2019. Proton-induced reactions on Fe, Cu, & Ti from threshold to 55 MeV. arXiv:1910.11135.

Werner, C.J., Bull, J.S., Solomon, C.J., Brown, F.B., McKinney, G.W., Rising, M.E., Dixon, D.A., Martz, R.L., Hughes, H.G., Cox, L.J., Zukaitis, A.J., Armstrong, J.C., Forster, R.A., Casswell, L., 2018. MCNP Version 6.2 Release Notes. Report LA-UR-18-20808, Los Alamos National Laboratory, http://dx.doi.org/10.2172/1419730.

Williams, H.A., Robinson, S., Julyan, P., Zweit, J., Hastings, D., 2005. A comparison of PET imaging characteristics of various copper radioisotopes. Eur. J. Nucl. Med. Mol. Imaging 32 (12), 1473–1480. http://dx.doi.org/10.1007/s00259-005-1906-9.

Zuber, K., Singh, B., 2015. Nuclear data sheets for A = 61. Nucl. Data Sheets 125, 1–200. http://dx.doi.org/10.1016/j.nds.2015.02.001.

Zweit, J., Smith, A.M., Downey, S., Sharma, H.L., 1991. Excitation functions for deuteron induced reactions in natural nickel: Production of no-carrier-added ^{64}Cu from enriched ^{64}Ni targets for positron emission tomography. Int. J. Radiat. Appl. Instrum. A 42 (2), 193–197. http://dx.doi.org/10.1016/0883-2889(91)90073-A.